A second-order ghost-fluid method for the primary atomization of liquid fuel in air-blast type injectors

By V. Moureau† AND O. Desjardins‡

This paper addresses the development of a novel method to handle high-density ratios in the computation of interfacial two-phase flows. This study is part of a larger effort, which aims at designing numerical solvers capable of computing the primary atomization of fuel by high-speed air. State-of-the-art methods for two-phase flows have shown their capability of computing primary atomization of high-speed liquids in quiescent gas with density ratios up to 50. These methods usually fail when the liquid is atomized by high-speed air or when the density ratio increases. In this paper, a new ghost-fluid method (GFM) of higher order is derived and verified. This method is then applied in the primary atomization of a low-speed water jet by a high-speed air coflow. All results show the potential of this second-order GFM for this type of flow.

1. Introduction

While Large-Eddy Simulation (LES) has demonstrated its potential for single-phase reacting flows in modern combustors (Boudier *et al.* 2007; Mahesh *et al.* 2006), two-phase flow LES are limited to dispersed sprays and do not take into account primary atomization. As a result, these two-phase computations are highly dependent on the boundary conditions imposed for the liquid phase, which are mainly the size and velocity distributions for the fuel droplets.

Primary atomization modeling is very challenging because it consists of unsteady topology changes of the liquid-gas interface, which have to be accurately represented. This process is also numerically challenging because of the discontinuous material properties of the two phases. As an example, the density jump at the interface can be of the order of 800 for the atomization of a water jet in air, or of the order of 1000 for liquid fuel atomized by air in a gas turbine undergoing light-on in altitude and cold conditions. Moreover, viscosity is also discontinuous at the interface, and surface tension creates a pressure jump where the interface is curved, leading to other discontinuities in the partial derivatives of the Navier-Stokes equations.

Several methods have been developed to model primary atomization. The most widely used and promising for turbulent atomization are the volume-of-fluid (VOF) (Scardovelli & Zaleski 1999) and level set (LS) (Sethian 1999; Osher & Fedkiw 2003) methods. These methods suffer from various drawbacks: while VOF methods are complex and of limited order of convergence for the interface transport, LS methods are usually plagued by spurious mass conservation errors. VOF and LS may be coupled to benefit from the advantages of each method but the resulting algorithm is even more complex. Recently,

† TURBOMECA SA, SAFRAN Group, France, and CORIA, CNRS-UMR-6614, France
‡ Mechanical Engineering Department, University of Colorado at Boulder, Colorado, USA

Desjardins *et al.* (2008*b*) developed an accurate, fully implicit and simple LS method, which conserves mass discretely. This accurate conservative level set (ACLS) approach combines the concept of conservative LS introduced by Olsson *et al.* (Olsson & Kreiss 2005; Olsson *et al.* 2007) with high-order implicit transport schemes in order to conserve mass while maximizing accuracy and robustness. The coupling with the flow solver is achieved due to the ghost-fluid method (GFM) (Fedkiw *et al.* 1999).

The LS method of Desjardins *et al.* (2008*b*) has been successfully applied in the computation of the atomization of a diesel jet with realistic material properties. Even if the Reynolds and Weber numbers were decreased to make the computation affordable, the main atomization phenomena were observed: capillary waves, ligament and drop formation, air entrainment. For this diesel jet, the liquid fuel was injected at high speed in quiescent air, and the momentum was mainly transferred from the liquid to the gas. At the gas-liquid interface, because of the density difference, the air was rapidly set in motion, and the tangential velocity continuity at the interface was preserved.

In air-blast injectors, in which the air has a high velocity compared to the liquid, the behavior of the gas is different. Indeed, the velocity gradient at the interface creates a thin boundary layer in the gas phase. Resolving this boundary layer is out of reach with usual LES meshes of injectors, and the numerical errors at the interface in the momentum equation may be important or even lead to numerical instability. Hence, limiting numerical errors is essential, especially in the case of air-blast atomization.

In this paper, a second-order GFM is presented. This method is an improvement of the original GFM, which is only first-order at the interface. Then, this method is verified for a 1-D test case and applied in the turbulent primary atomization of water by high-speed air.

2. The accurate conservative level set (ACLS)

In this section, the ACLS method developed by Desjardins *et al.* (2008*b*), which is a combination of the conservative level set method and the GFM, is described.

2.1. *The conservative level set method*

The method used in this study is derived from the Conservative Level Set (CLS) of Olsson *et al.* (Olsson & Kreiss 2005; Olsson *et al.* 2007). The time advancement of the CLS consists of two steps. The first step is a transport step of the level set ψ at the flow velocity $\mathbf{u}$:

$$\frac{\partial \psi}{\partial t} + \nabla \cdot (\psi \mathbf{u}) = 0\,. \tag{2.1}$$

The second step is a re-initialization step. In this step, a partial differential equation is advanced in pseudo-time τ:

$$\frac{\partial \psi}{\partial \tau} + \nabla \cdot (\psi(1-\psi)\mathbf{n}) = \nabla \cdot (\epsilon(\nabla\psi \cdot \mathbf{n})\mathbf{n})\ , \tag{2.2}$$

where $\mathbf{n}$ is the normal to the interface, and ϵ is a diffusion coefficient, which is related to the thickness of the level set function.

The combination of these two steps ensures that the level set is transported at the velocity $\mathbf{u}$, and that the level set retains a hyperbolic tangent profile:

$$\psi(\mathbf{x}, t) = \frac{1}{2}\left(\tanh\left(\frac{\phi(\mathbf{x}, \mathrm{t})}{2\epsilon}\right) + 1\right)\ , \tag{2.3}$$

where ϕ is the signed distance to the interface. With this profile, the level set is located at $\psi = 0.5$, which is equivalent to $\phi = 0$. The CLS method needs an accurate definition of the interface normal $\mathbf{n}$ to limit the spurious interface displacements that could be caused by the re-initialization. The originality of the Accurate Conservative Level Set (ACLS) (Desjardins *et al.* 2008*b*) method is to rely on ϕ to compute the normals instead of ψ. This necessitates the building of ϕ before the re-initialization, and this is achieved via the Fast Marching Method (Sethian 1999). Since the normals are computed from ϕ and not ψ, the low-order non-oscillatory schemes used by Olsson *et al.* in order to ensure robustness become unnecessary and can be replaced by high-order accurate implicit schemes. The resulting ACLS method retains the mass conservation property of the CLS method, but provides significant improvements over CLS in terms of both robustness and accuracy.

2.2. *The first-order ghost-fluid method (GFM)*

2.2.1. *The principle of the GFM*

Following Delhaye (1974), the velocity in both phases is continuous at the interface for atomizing sprays provided evaporation is negligible. This is not the case for the pressure which exhibits a jump because of surface tension force and viscous stresses, and for the pressure gradient due to the density jump. Hence, the usual discrete operators for gradient and Laplacian of the pressure are not usable because they rely on Taylor series expansions that are not valid in the presence of jumps.

A solution to this issue consists in expanding both phases to the other sides of the interface. This enables the removal of the discontinuities and the computation of the discrete operators in the same phase even across the interface. This is achieved by performing Taylor series expansions of both phases from the interface Γ. For the pressure P, this is written

$$P_l(\mathbf{x}) = P_{l,\Gamma} + (\mathbf{x} - \mathbf{x}_\Gamma) \cdot \nabla P|_{l,\Gamma} + \mathcal{O}\left((\mathbf{x} - \mathbf{x}_\Gamma)^2\right) , \tag{2.4}$$

$$P_g(\mathbf{x}) = P_{g,\Gamma} + (\mathbf{x} - \mathbf{x}_\Gamma) \cdot \nabla P|_{g,\Gamma} + \mathcal{O}\left((\mathbf{x} - \mathbf{x}_\Gamma)^2\right) , \tag{2.5}$$

where the l, g and Γ subscripts refer to the liquid, the gas and the interface, respectively. The variable $\mathbf{x}$ represents the coordinates and $\mathbf{x}_\Gamma$ is the position of the interface. Subtracting the two previous equations defines the pressure jump $[P]$ extended in both phases away from the interface:

$$[P](\mathbf{x}) = [P]_\Gamma + (\mathbf{x} - \mathbf{x}_\Gamma) \cdot [\nabla P]_\Gamma + \mathcal{O}\left((\mathbf{x} - \mathbf{x}_\Gamma)^2\right) . \tag{2.6}$$

The pressure jump at the interface $[P]_\Gamma$ is due to the surface tension and the viscous stresses:

$$[P]_\Gamma = \sigma\kappa + 2[\mu]_\Gamma \, \mathbf{n}^t \cdot \nabla\mathbf{u} \cdot \mathbf{n} , \tag{2.7}$$

where $\mathbf{n}$ is the interface normal, σ is the surface tension, $\kappa = -\nabla \cdot \mathbf{n}$ is the interface curvature, and $[\mu]_\Gamma$ is the dynamic viscosity jump. The pressure gradient jump can be computed by noting that the pressure gradient weighted by the density inverse has to be continuous for the velocity to be continuous:

$$\left[\frac{1}{\rho}\nabla P\right]_\Gamma = 0 , \tag{2.8}$$

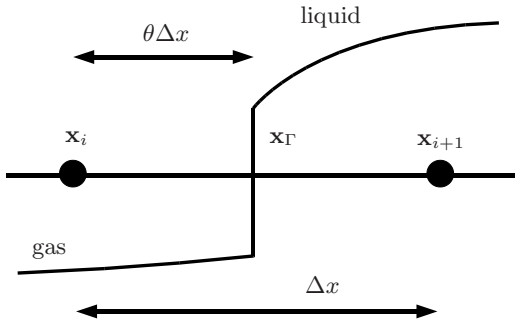

FIGURE 1. Sketch of the subcell interface location between two nodes, and notations.

then

$$[\nabla P]_\Gamma = [\rho]\ \frac{1}{\rho_g}\nabla P\bigg|_{g,\Gamma} = [\rho]\ \frac{1}{\rho_l}\nabla P\bigg|_{l,\Gamma} . \tag{2.9}$$

2.2.2. *Notations*

The notations used in the following derivations are given in Fig. 1. In this figure, the interface Γ is located between the nodes i and $i+1$. The distance between the two nodes is $\Delta x = |\mathbf{x}_{i+1} - \mathbf{x}_i|$. Then, the fraction of the distance between this node pair in the gas is written $\theta = |\mathbf{x}_\Gamma - \mathbf{x}_i|/\Delta x$. With this gas fraction, a weighted density can be defined,

$$\rho^\star = \theta\rho_g + (1-\theta)\rho_l\,. \tag{2.10}$$

Finally, the node pair direction $\mathbf{d}_{i+1/2}$ can also be introduced,

$$\mathbf{d}_{i+1/2} = \frac{\mathbf{x}_{i+1} - \mathbf{x}_i}{\Delta x}\,. \tag{2.11}$$

2.2.3. *Jump conditions away from the interface for a discrete field*

From the known pressure and pressure gradient jumps, the pressure field of each phase can be extended on both sides of the interface. This allows the definition of the usual discrete operators everywhere, including across the interface. Following the notations of Fig. 1, it is assumed that a node i of the mesh is in the gas, and a neighboring node $i+1$ is in the liquid. Then, the gas pressure at $i+1$ is simply equal to the liquid pressure minus the jump condition at $i+1$,

$$P_{g,i+1} = P_{l,i+1} - [P]_{i+1}\,. \tag{2.12}$$

From Eqs. (2.6) and (2.9), the pressure jump at $i+1$ can be expressed from the interface jumps by

$$[P]_{i+1} = [P]_\Gamma + (\mathbf{x}_{i+1} - \mathbf{x}_\Gamma)\cdot[\rho]\frac{1}{\rho_g}\ \nabla P|_{g,\Gamma} + \mathcal{O}\left((\mathbf{x}_{i+1} - \mathbf{x}_\Gamma)^2\right)\,. \tag{2.13}$$

In Eq. (2.13), the pressure gradient in the gas $\nabla P|_{g,\Gamma}$ in the $\mathbf{d}_{i+1/2}$ direction can be computed from known quantities. Centered finite differencing is adopted for this pressure gradient, leading to

$$\mathbf{d}_{i+1/2}\cdot\nabla P|_{g,\Gamma} = \frac{P_{l,i+1} - [P]_{i+1} - P_{g,i}}{\Delta x} + \mathcal{O}\left((\mathbf{x}_{i+1} - \mathbf{x}_i)\right)\,. \tag{2.14}$$

From Eqs. (2.13) and (2.14), the pressure jump at node $i+1$ takes the form

$$[P]_{i+1} = [P]_\Gamma + (1-\theta)[\rho]\frac{1}{\rho_g}\left(P_{l,i+1} - [P]_{i+1} - P_{g,i}\right) + \mathcal{O}\left((\mathbf{x}_{i+1} - \mathbf{x}_\Gamma)^2\right) . \tag{2.15}$$

Equation (2.15) can be inverted to obtain the pressure jump $[P]_{i+1}$. Then, the pressure jump $[P]_{i+1}$ is simply expressed from the pressure jump at the interface $[P]_\Gamma$, the weighted density $\rho^\star$, and the pressure at nodes i and $i+1$ in each phase,

$$[P]_{i+1} = \frac{\rho_g}{\rho^\star}[P]_\Gamma + \left(1 - \frac{\rho_g}{\rho^\star}\right)\left(P_{l,i+1} - P_{g,i}\right) + \mathcal{O}\left((\mathbf{x}_{i+1} - \mathbf{x}_\Gamma)^2\right) . \tag{2.16}$$

Following the same methodology, the pressure jump can be computed in the liquid at node i

$$[P]_i = \frac{\rho_l}{\rho^\star}[P]_\Gamma + \left(1 - \frac{\rho_l}{\rho^\star}\right)\left(P_{l,i+1} - P_{g,i}\right) + \mathcal{O}\left((\mathbf{x}_\Gamma - \mathbf{x}_i)^2\right) . \tag{2.17}$$

2.2.4. *Derivation of the pressure gradient operator*

Knowing the pressure jump at $[P]_{i+1}$ is sufficient to build discrete operators for the pressure derivatives. For instance, the pressure gradient in the gas in the direction $\mathbf{d}_{i+1/2}$ weighted by the inverse of the density is equal to

$$\mathbf{d}_{i+1/2} \cdot \frac{1}{\rho}\nabla P\bigg|_{g,i+1/2} = \frac{1}{\rho_g}\frac{P_{g,i+1} - P_{g,i}}{\Delta x} + \mathcal{O}\left(\Delta x\right) , \tag{2.18}$$

$$= \frac{1}{\rho_g}\frac{P_{l,i+1} - [P]_{i+1} - P_{g,i}}{\Delta x} + \mathcal{O}\left(\Delta x\right) , \tag{2.19}$$

$$= \frac{1}{\rho^\star}\frac{P_{l,i+1} - P_{g,i}}{\Delta x} - \frac{1}{\rho^\star}\frac{[P]_\Gamma}{\Delta x} + \mathcal{O}\left(\Delta x\right) . \tag{2.20}$$

The pressure gradient in the liquid can be expressed in the same fashion,

$$\mathbf{d}_{i+1/2} \cdot \frac{1}{\rho}\nabla P\bigg|_{l,i+1/2} = \frac{1}{\rho_l}\frac{P_{l,i+1} - P_{l,i}}{\Delta x} + \mathcal{O}\left(\Delta x\right) , \tag{2.21}$$

$$= \frac{1}{\rho_l}\frac{P_{l,i+1} - P_{g,i} - [P]_i}{\Delta x} + \mathcal{O}\left(\Delta x\right) , \tag{2.22}$$

$$= \frac{1}{\rho^\star}\frac{P_{l,i+1} - P_{g,i}}{\Delta x} - \frac{1}{\rho^\star}\frac{[P]_\Gamma}{\Delta x} + \mathcal{O}\left(\Delta x\right) , \tag{2.23}$$

which is the same expression as Eq. (2.20). This proves that this operator discretely satisfies the right jump condition for the pressure gradient weighted by the inverse of the density, which has to be zero, i.e.,

$$\left[\frac{1}{\rho}\nabla P\right]_{i+1/2} = \frac{1}{\rho}\nabla P\bigg|_{l,i+1/2} - \frac{1}{\rho}\nabla P\bigg|_{g,i+1/2} = 0 . \tag{2.24}$$

3. A second-order ghost-fluid method

The first-order GFM gives reasonable results for flows with low density ratios or when the kinetic energy is dominant in the liquid. For high density ratios and liquid fuel atomized by high-speed air, the first-order GFM exhibits numerical instabilities. This is partly due to the errors introduced by the first-order GFM at the interface in the pressure gradient, which lead to spurious inertia forces. To improve the GFM and reduce these

errors, the order of the GFM can be increased. This section presents the derivation of a second-order GFM.

In order to derive a second-order GFM, the order of the Taylor series expansion of the jump conditions away from the interface given in Eq. (2.6) is increased, which gives

$$[P](\mathbf{x}) = [P]_\Gamma + (\mathbf{x}-\mathbf{x}_\Gamma)\cdot[\nabla P]_\Gamma + \frac{1}{2}(\mathbf{x}-\mathbf{x}_\Gamma)^t\cdot[\nabla\nabla P]_\Gamma\cdot(\mathbf{x}-\mathbf{x}_\Gamma) + \mathcal{O}\left((\mathbf{x}-\mathbf{x}_\Gamma)^3\right) . \quad (3.1)$$

The pressure gradient jump can be expressed as a function of the gradient in one of the phases using Eq. (2.9). An additional assumption is needed to calculate the jump of the pressure Hessian. Assuming that the velocity derivatives are continuous at the interface requires that the pressure Hessian weighted by the inverse of the density is also continuous. This hypothesis leads to a relation similar to Eq. (2.9),

$$[\nabla\nabla P]_\Gamma = [\rho]\left.\frac{1}{\rho_g}\nabla\nabla P\right|_{g,\Gamma} = [\rho]\left.\frac{1}{\rho_l}\nabla\nabla P\right|_{l,\Gamma} . \quad (3.2)$$

Applying Eqs. (3.1), (2.9) and (3.2) to the nodes i in the gas and $i+1$ in the liquid gives the following pressure jump at node $i+1$,

$$[P]_{i+1} = [P]_\Gamma + (\mathbf{x}_{i+1}-\mathbf{x}_\Gamma)\cdot[\rho]\left.\frac{1}{\rho_g}\nabla P\right|_{g,\Gamma} + \frac{1}{2}(\mathbf{x}_{i+1}-\mathbf{x}_\Gamma)^t\cdot[\rho]\left.\frac{1}{\rho_g}\nabla\nabla P\right|_{g,\Gamma}\cdot(\mathbf{x}_{i+1}-\mathbf{x}_\Gamma) + \mathcal{O}\left((\mathbf{x}_{i+1}-\mathbf{x}_\Gamma)^3\right) . \quad (3.3)$$

In the previous equation, the pressure gradient in the gas at the interface cannot be expressed directly from known quantities while maintaining the desired accuracy, as done for the first-order GFM. First, this gradient has to be computed from the pressure gradient at $i+1/2$ between the nodes i and $i+1$,

$$\left.\frac{1}{\rho_g}\nabla P\right|_{g,\Gamma} = \left.\frac{1}{\rho_g}\nabla P\right|_{g,i+1/2} + (\mathbf{x}_\Gamma-\mathbf{x}_{i+1/2})^t\cdot\left.\frac{1}{\rho_g}\nabla\nabla P\right|_{g,i+1/2} + \mathcal{O}\left((\mathbf{x}_\Gamma-\mathbf{x}_{i+1/2})^2\right) . \quad (3.4)$$

After combining Eqs (3.3), (3.4) and (2.14), and inverting the resulting relation, one finally obtains the pressure jump at node $i+1$ for the second-order GFM,

$$[P]_{i+1} = \frac{\rho_g}{\rho^\star}[P]_\Gamma + \left(1-\frac{\rho_g}{\rho^\star}\right)(P_{i+1,l}-P_{i,g}) + \frac{\rho_g}{\rho^\star}\frac{\Delta x^2}{2}[\rho]\theta(1-\theta)\,\mathbf{d}_{i+1/2}^t\cdot\left.\frac{1}{\rho}\nabla\nabla P\right|_{i+1/2}\cdot\mathbf{d}_{i+1/2} + \mathcal{O}\left((\mathbf{x}_{i+1}-\mathbf{x}_\Gamma)^3\right) . \quad (3.5)$$

A similar relation may be obtained for the pressure jump at node i,

$$[P]_i = \frac{\rho_l}{\rho^\star}[P]_\Gamma + \left(1-\frac{\rho_l}{\rho^\star}\right)(P_{i+1,l}-P_{i,g}) + \frac{\rho_l}{\rho^\star}\frac{\Delta x^2}{2}[\rho]\theta(1-\theta)\,\mathbf{d}_{i+1/2}^t\cdot\left.\frac{1}{\rho}\nabla\nabla P\right|_{i+1/2}\cdot\mathbf{d}_{i+1/2} + \mathcal{O}\left((\mathbf{x}_\Gamma-\mathbf{x}_i)^3\right) . \quad (3.6)$$

Finally, the pressure gradient in the gas or in the liquid for the pair of nodes i and

$i+1$ in the direction $\mathbf{d}_{i+1/2}$ can be computed as follows:

$$\mathbf{d}_{i+1/2}\cdot\frac{1}{\rho}\nabla P\bigg|_{l,i+1/2}=\mathbf{d}_{i+1/2}\cdot\frac{1}{\rho}\nabla P\bigg|_{g,i+1/2}=\frac{1}{\rho^\star}\frac{P_{i+1,l}-P_{i,g}}{\Delta x}$$
$$-\frac{1}{\rho^\star\Delta x}\left([P]_\Gamma+\frac{\Delta x^2}{2}[\rho]\theta(1-\theta)\,\mathbf{d}^t_{i+1/2}\cdot\frac{1}{\rho}\nabla\nabla P\bigg|_{i+1/2}\cdot\mathbf{d}_{i+1/2}\right)+\mathcal{O}(\Delta x^2)\,. \quad (3.7)$$

In the latter equation, the Hessian may be evaluated from the pressure gradient at the previous time step or at the previous iteration by

$$\mathbf{d}^t_{i+1/2}\cdot\frac{1}{\rho}\nabla\nabla P\bigg|_{i+1/2}\cdot\mathbf{d}_{i+1/2}=\frac{\frac{1}{\rho}\nabla P\Big|_{i+1}-\frac{1}{\rho}\nabla P\Big|_{i}}{\Delta x}\cdot\mathbf{d}_{i+1/2}+\mathcal{O}(\Delta x^2)\,. \quad (3.8)$$

Compared to the first-order GFM, the second-order GFM has an additional term with the pressure Hessian. This term resembles the pressure jump at the interface $[P]_\Gamma$. This method can therefore be implemented similarly to the first-order GFM, but with a modified pressure jump at the interface $[P]'_\Gamma$, which is written

$$[P]'_\Gamma=[P]_\Gamma+\frac{\Delta x^2}{2}[\rho]\theta(1-\theta)\,\mathbf{d}^t_{i+1/2}\cdot\frac{1}{\rho}\nabla\nabla P\bigg|_{i+1/2}\cdot\mathbf{d}_{i+1/2}\,. \quad (3.9)$$

4. Verification

To verify the second-order GFM and compare its performance against its first-order counterpart, the two methods are used to compute the pressure gradient weighted by the density inverse for a family of 1-D manufactured solutions. These solutions satisfy the following jump conditions: $[P]_\Gamma=100$, $[\rho^{-1}\nabla P]_\Gamma=0$ and $[\rho^{-1}\nabla\nabla P]_\Gamma=0$, and are defined as follows:

$$P(x)=\begin{cases}\rho_g\phi(x) & \text{if } x<x_\Gamma,\\ \rho_g\phi(x_\Gamma)+\rho_l\left(\phi(x)-\phi(x_\Gamma)\right)+[P]_\Gamma & \text{else,}\end{cases} \quad (4.1)$$

where the function ϕ is an infinitely differentiable function, $\rho_g=1$, and $\rho_l=1000$. According to the definition of the manufactured solution, the pressure gradient weighted by the density inverse is simply:

$$\frac{1}{\rho}\frac{\partial P}{\partial x}\bigg|_l=\frac{1}{\rho}\frac{\partial P}{\partial x}\bigg|_g=\frac{\partial\phi}{\partial x}\,. \quad (4.2)$$

From this family of manufactured solutions, two functions ϕ are chosen to assess the performances of the method. The first is a second-order polynomial with $\phi(x)=x^2$ and the second is a third-order polynomial, i.e., $\phi(x)=x^3$. For these two cases, the interface is located at $x_\Gamma=1\cdot10^{-3}$. The pressure profiles for the two cases are represented in Fig. 2.

The computation of the gradient is performed on a uniform mesh with a second-order finite-difference scheme away from the interface, with Eq. (2.20) for the first-order GFM, and with Eq. (3.7) for the second-order GFM across the interface. The pressure Hessian in the second-order GFM is pre-computed using the first-order GFM. The L_∞ norm of the error between the analytical solution and the computed solution is calculated for different mesh resolutions; the results are presented in Table 1 for the second-order polynomial and in Table 2 for the third-order polynomial. These results clearly highlight the

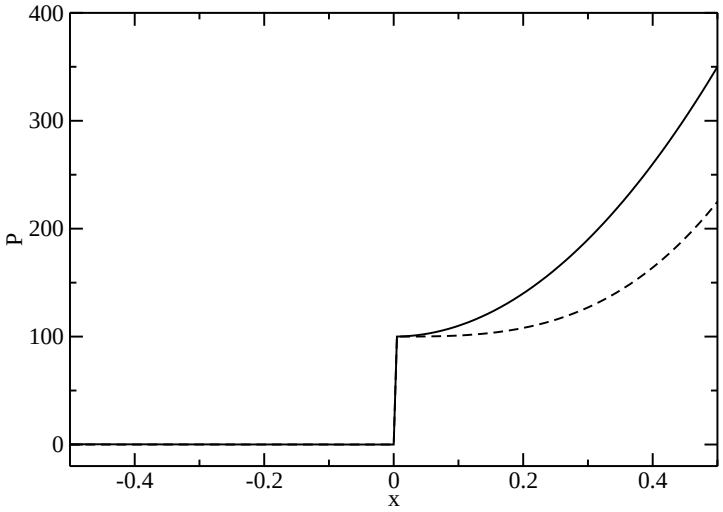

FIGURE 2. Pressure profiles. ——— : second-order polynomial ; – – – – : third-order polynomial.

Δx (mm)	First-order GFM L_∞ norm	Second-order GFM L_∞ norm
0.005	4.99375E-004	7.93530E-013
0.01	4.99445E-004	1.65974E-013
0.02	4.99474E-004	2.33239E-014
0.05	9.46622E-003	2.27249E-014

TABLE 1. Second-order polynomial.

Δx (mm)	First-order GFM L_∞ norm	Second-order GFM L_∞ norm
0.005	2.79963E-005	2.50000E-005
0.01	1.05494E-004	1.00000E-004
0.02	4.10489E-004	4.00000E-004
0.05	7.44023E-003	2.50000E-003

TABLE 2. Third-order polynomial.

benefits of the second-order GFM. For a second-order polynomial, the pressure gradient shows machine accuracy with the second-order GFM, while for the first-order GFM, the error is not negligible and can be a source of spurious inertia forces in more complex computations. In the case of the third-order polynomial, the error is due to both the interface jumps and to the second-order finite-difference scheme, which is not exact for a third-order polynomial. Nevertheless, with the second-order GFM, only the error of the finite-difference scheme is seen, while for the first-order GFM, the error due to the jump conditions is negligible for the fine meshes but becomes dominant for coarse meshes. Again, the second-order GFM leads to a significant improvement.

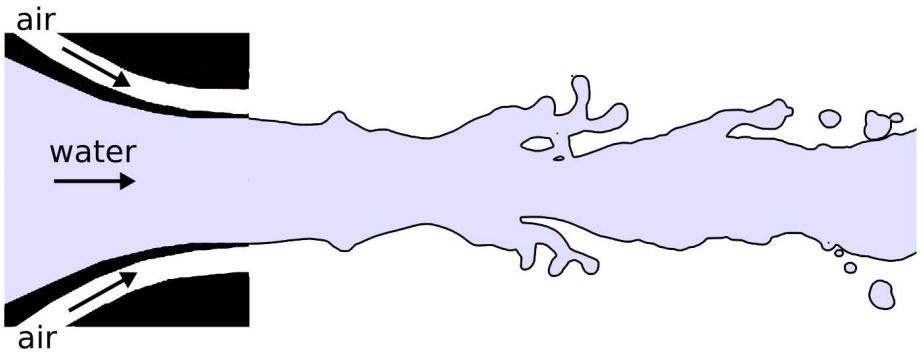

FIGURE 3. Sketch of the experiment.

5. Validation of the second-order GFM for a liquid jet

In this section, the second-order GFM is validated for a low-speed liquid jet surrounded by a coflow of high-speed air. This case was first carried out with the first-order GFM but all of the computations diverged before exhibiting interesting features. The numerical instabilities were occurring specifically in the regions where the gas was able to entrain a certain amount of liquid. This issue motivated the development of the second-order GFM to improve the robustness and the accuracy of the solver at the interface, in the presence of strong tangential velocity gradients.

5.1. *Description of the experiment*

The experiment consists of a round jet of low-speed water atomized by an annular high-speed air stream. This experiment has been used extensively by Lasheras & Hopfinger (2000) and Marmottant & Villermaux (2004) to study the break-up regimes and the mechanisms of the formation of drops and ligaments. A sketch of the experimental setup is given in Fig. 3; additional details about the experimental conditions can be found in Lasheras & Hopfinger (2000) and Marmottant & Villermaux (2004). The inner diameter and the annulus gap width are 7.8 mm and 1.7 mm, respectively. Several sets of parameters for the inflow conditions are available in these papers, but only one set was computed in the present work. The chosen inlet velocities for the gas and liquid are $u_g = 21\,\mathrm{m/s}$ and $u_l = 0.55\,\mathrm{m/s}$. For these velocities, the gas Weber number is 58, meaning that surface tension effects are dominant, and the Reynolds number in the gas and in the liquid are 3000 and 3760, indicating that the two jets are turbulent. Finally, the momentum flux ratio of the two streams is $M = \rho_g u_g^2/(\rho_l u_l^2) = 1.76$. This means that a transfer of momentum from the gas to the liquid should occur.

5.2. *Description of the solvers*

Two different codes called NGA and YALES2 were used for this study. NGA is a 3-D structured code based on fully conservative finite-difference schemes of arbitrary order (Desjardins *et al.* 2008*a*). It solves the incompressible Navier-Stokes equations using a fractional-step method (Kim & Moin 1985). YALES2 is a 1-D, 2-D and 3-D unstructured code for hybrid grids that relies on central finite-volume schemes of fourth-order in space. It also solves the incompressible Navier-Stokes equations using a fractional-step method. Both codes are parallel and rely on the Message Passing Interface (MPI), with the capability of running on a large number of processors. NGA is based on 3-D domain decomposition, and YALES uses a double decomposition method with a first partition-

ing into N parts, where N is the number of processors, then the mesh is partitioned again into cell groups that fit in the cache memory. For this problem, the Poisson solver used in NGA was a parallel conjugate gradient scheme preconditioned by a geometric multi-grid method, part of the Hypre library (Falgout *et al.* 2005), while YALES used a BiCGStab(2) solver (Van der Vorst 1995).

5.3. *High-order shock capturing*

To compute two-phase flows with high-density ratios and complex dynamics, it was found necessary to use a shock-capturing technique in order to stabilize the computations. This is partly due to the fact that all the spatial schemes in NGA and YALES2 are centered, and may therefore generate spurious dispersion errors. The shock-capturing technique employed in both codes is similar to the method of Cook & Cabot (2004). A fourth-order artificial viscosity is added to the dynamic viscosity in each phase and is defined as follows:

$$\mu_{\text{artif}} = \rho C_\mu \Delta x^5 \left| \Delta\nabla \cdot \left(\nabla \mathbf{u} + \nabla \mathbf{u}^t \right) \right| , \tag{5.1}$$

where $C_\mu = 0.1$, and the characteristic cell size Δx is simply related to the cell volume V by $\Delta x = V^{1/3}$. The value of C_μ chosen in these computations is equal to the value used by Cook & Cabot (2004). Nevertheless, the influence of the shock capturing technique on two-phase computations was checked for simple test cases with analytic solutions, such as capillarity instabilities, and it was found that it was negligible compared to the numerical errors of the finite-difference and finite-volume schemes.

5.4. *Results*

The computation of the experiment was carried out with a tetrahedron-based mesh of 18.5 million cells. The characteristic cell size in the vicinity of the gas and liquid inlets is approximately 0.15 mm with finer cells around 0.1 mm at the lip between the two fluids. This cell size may be compared to a Kolmogorov scale in the liquid jet of the order of 40 μm, which indicates that almost all the scales inside the liquid jet are resolved on the mesh. In the gas, the Kolmogorov scale is approximately 10 μm, indicating that only the smallest scales are not resolved. The initialization was done with a conic liquid core, which was 7.9 liquid diameters long.

The results obtained with YALES2 are shown in Figs. 4 and 5. In these two figures, the interface is represented as an iso-contour of the level set. Figure 4 highlights the high level of dynamics in the jets. Because of the momentum ratio, which is in favor of the gas, the liquid is entrained in some regions by recirculating vortices of gas. In these high-shear regions, ligaments are formed and eventually lead to the formation of large drops. These zones and the resulting ligaments are well represented in Fig. 5, where the velocity field is also plotted. These results can be compared to the photographs of Lasheras & Hopfinger (2000) for the same inlet velocities. The first notable difference is that the computation exhibits more ligaments that are also finer. This is due to the fact that this flow is highly dependent upon surface tension forces, and these forces need a very accurate calculation of the curvature. The numerics used in this study to compute the interface curvature are not accurate enough, and they introduce spurious high-frequency errors in the curvature. Therefore, the order of convergence of the curvature calculation must be increased in order to improve the results. The second difference between the computation and the experiment is in the injection plane. In the computation, the gas partly recirculates inside the pipe of the liquid jet. This may be due to the lack of resolution in the lip between the two streams. The thickness of the lip is 0.2 mm and only

FIGURE 4. 3-D view of the interface location at $t = 6\,\text{ms}$.

FIGURE 5. Planar cut of the velocity field and of the interface location at $t = 6\,\text{ms}$.

two cells were used to discretize it. More generally, Marmottant & Villermaux (2004) underlined that the mixing layer thickness between the gas and the liquid, imposed by the thickness of the lip, has a strong influence on the first structures observed after the injection plane. These structures are the most energetic, because in this region the jets are still coherent, and they need to be well-predicted to obtain the formation of the first ligaments.

6. Conclusions

In this paper, a novel ghost-fluid method (GFM) is presented. While the original GFM is first order at the interface, the new method is second order and was verified for a manufactured solution. Then, the method was applied in the computation of a low-speed water jet atomized by a high-speed air stream. The second-order GFM proves to be more stable than its first-order counterpart for two-phase flows with high density ratios. Nevertheless, several points need to be addressed before obtaining a good comparison between the experiments and the computation. The most important is improving the accuracy of the curvature computation to model the surface tension forces correctly, and to refine the mesh at the lip between the gas and the liquid.

Acknowledgements

The authors gratefully acknowledge Dr. Guillaume Blanquart's valuable comments on this manuscript.

REFERENCES

Boudier, G., Gicquel, L., Poinsot, T., Bissières, D. & Bérat, C. 2007 Comparison of LES, RANS and experiments in an aeronautical gas turbine combustion chamber. *In Proc. of the Combustion Institute* **31** (2), 3075–3082.

Cook, A. & Cabot, W. 2004 A high-wavenumber viscosity for high-resolution numerical methods. *J. Comp. Physics* **195** (2), 594–601.

Delhaye, J. 1974 Jump conditions and entropy sources in two-phase systems. Local instant formulation. *Int. J. Multiphase Flow* **1**, 395–409.

Desjardins, O., Blanquart, G., Balarac, G. & Pitsch, H. 2008*a* High order conservative finite difference scheme for variable density low Mach number turbulent flows. *J. Comp. Physics* **227** (15), 7125–7159.

Desjardins, O., Moureau, V. & Pitsch, H. 2008*b* An accurate conservative level set/ghost fluid method for simulating turbulent atomization. *J. Comp. Physics* **227** (18), 8395–8416.

Falgout, R., Jones, J. & Yang, U. 2005 The design and implementation of hypre, a library of parallel high performance preconditioners. *Lecture Notes in Computational Science and Engineering* **51**, 267.

Fedkiw, R. P., Aslam, T., Merriman, B. & Osher, S. 1999 A non-oscillatory eulerian approach to interfaces in multimaterial flows (the ghost fluid method). *J. Comput. Phys.* **152** (2), 457–492.

Kim, J. & Moin, P. 1985 Application of a fractional-step method to incompressible Navier-Stokes equations. *J. Comp. Physics* **59**, 308–323.

Lasheras, J. & Hopfinger, E. 2000 Liquid jet instability and atomization in a coaxial gas stream. *Ann. Rev. Fluid Mech.* **32** (1), 275–308.

Mahesh, K., Constantinescu, G., Apte, S., Iaccarino, G., Ham, F. & Moin, P. 2006 Large-eddy simulation of reacting turbulent flows in complex geometries. *J. Applied Mechanics* **73** (3), 374–381.

Marmottant, P. & Villermaux, E. 2004 On spray formation. *J. Fluid Mech.* **498**, 73–111.

Olsson, E. & Kreiss, G. 2005 A conservative level set method for two phase flow. *J. Comput. Phys.* **210** (1), 225–246.

Olsson, E., Kreiss, G. & Zahedi, S. 2007 A conservative level set method for two phase flow ii. *J. Comput. Phys.* **225** (1), 785–807.

Osher, S. & Fedkiw, R. 2003 *Level set methods and dynamic implicit interfaces*. New York: Springer.

Scardovelli, R. & Zaleski, S. 1999 Direct numerical simulation of free-surface and interfacial flow. *Ann. Rev. Fluid Mech.* **31**, 567–603.

Sethian, J. A. 1999 *Level set methods and fast marching methods*, second ed. Cambridge, U.K.: Cambridge University Press.

Van der Vorst, H. 1995 Parallel iterative solution methods for linear systems arising from discretized PDE's. *Agard Reports* **3** (1), 1–39.